

Synthetic Abundance Maps for Unsupervised Super-Resolution of Hyperspectral Remote Sensing Images

Xinxin Xu, Yann Gousseau, Christophe Kervazo, Saïd Ladjal

Abstract—Hyperspectral single image super-resolution (HS-SISR) aims to enhance the spatial resolution of hyperspectral images to fully exploit their spectral information. While considerable progress has been made in this field, most existing methods are supervised and require ground truth data for training—data that is often unavailable in practice. To overcome this limitation, we propose a novel unsupervised training framework for HS-SISR, based on synthetic abundance data. The approach begins by unmixing the hyperspectral image into endmembers and abundances. A neural network is then trained to perform abundance super-resolution using synthetic abundances only. These synthetic abundance maps are generated from a dead leaves model whose characteristics are inherited from the low-resolution image to be super-resolved. This trained network is subsequently used to enhance the spatial resolution of the original image’s abundances, and the final super-resolution hyperspectral image is reconstructed by combining them with the endmembers. Experimental results demonstrate both the training value of the synthetic data and the effectiveness of the proposed method.

Index Terms—Hyperspectral image; remote sensing; super-resolution; unsupervised learning; synthetic training data

I. INTRODUCTION AND RELATED WORK

HYPERSPECTRAL images (HSI) are three-dimensional data structures, similar to multispectral and natural images, composed of two spatial dimensions and one spectral dimension. While natural images are typically acquired in three RGB bands and multispectral images in a few dozen bands, HSIs capture scenes across hundreds or even thousands of contiguous spectral bands, depending on the sensor. This high spectral resolution allows for fine-grained material discrimination and supports a wide range of applications, such as astrophysics [1], target detection [2], and numerous remote sensing tasks, which are of primary interest in the context of this work. In particular, HSIs have proven highly effective for vegetation monitoring [3], land use and land cover classification [4], to name a few.

Regardless of the application, hyperspectral data generally suffer from low spatial resolution due to the need to capture narrow spectral bands, which limits the amount of photons per pixel. To preserve a sufficient signal-to-noise ratio, sensors use larger pixels, which reduces spatial precision. This limitation is particularly critical in remote sensing, where the distance between the sensor and the scene further degrades spatial precision. To address this challenge, super-resolution techniques aim to improve the spatial resolution of HSIs while preserving their spectral consistency. Existing methods for hyperspectral super-resolution can be grouped into two main categories:

The authors are with LTCI, Télécom Paris, Institut Polytechnique de Paris, 91120 Palaiseau, France (e-mail: xinxin.xu@telecom-paris.fr; yann.gousseau@telecom-paris.fr; christophe.kervazo@telecom-paris.fr; said.ladjal@telecom-paris.fr).

MSI-HSI fusion : This strategy seeks to combine a high-spatial, low-spectral resolution multispectral image (MSI) with a low-spatial, high-spectral resolution HSI. A widely used intermediary step for this purpose is hyperspectral unmixing [5], which decomposes each pixel into a linear combination of endmembers (pure material spectral signatures) and their corresponding abundances [6]. The key idea is to extract the spatial details from the MSI (via its abundance) and to combine them with the spectral information provided by the endmembers of the HSI. Several deep learning-based methods have extended this principle. For example, HyCoNet [7] introduces a three-branch autoencoder structure capable of jointly estimating the point spread function (PSF) and spectral response function (SRF) from the data. More recently, Hong et al. [8] proposed a fusion architecture that decouples the MSI and HSI into common and sensor-specific components before recombining them in a shared feature space to produce a fused output image.

Single Image Super-Resolution (SISR) : In contrast to fusion methods, SISR approaches aim to reconstruct a high-spatial resolution HSI from a single low-spatial resolution observation, without relying on external guidance from an MSI. Early SISR techniques were model-driven. For instance, Akgun et al. [9] formulated super-resolution as an inverse problem, solved using Projection Onto Convex Sets (POCS) [10]. With the rise of deep learning, data-driven methods have become predominant. A common approach is to use Convolutional Neural Networks (CNNs) that can learn the mapping from low-to high-resolution directly from training data. Yuan et al. [11] leveraged transfer learning by training networks on natural images and adapting them to hyperspectral data. To better capture the intrinsic spatial-spectral correlations in HSIs, several network architectures have been designed to jointly process both domains. Early deep models either used fully 3D convolutions [12] to handle spectral cubes holistically, or decoupled spatial and spectral extraction via 1D (spectral) and 2D (spatial) convolutions [13]. More advanced designs propose hybrid schemes to balance performance and efficiency. For example, SSPSR [14] introduces a spatial-spectral residual block combining 2D convolutions and spectral attention, while adopting spectral grouping to reduce parameter overhead. HSISR [15] builds upon this by incorporating a parallel RGB super-resolution task, enabling shared spatial feature learning across modalities and semi-supervised training on unlabelled HSI data. MCNet [16] further develops this idea with a mixed 2D/3D convolutional architec-

ture, where spatial features are extracted via lightweight 2D convolutions and spectral dependencies are modeled through separable 3D convolutions within a unified residual framework.

Despite their potential, both fusion and SISR methods face critical limitations. Fusion techniques require precise spatial alignment between the MSI and HSI, which is difficult to achieve in practice and can introduce artifacts or performance degradation when misalignments occur. This issue is particularly acute in remote sensing, where, to the best of our knowledge, co-registered MSI and HSI pairs are not available. On the other hand, most SISR methods rely on supervised learning, which demands large datasets with known high-resolution ground truth. However, such datasets are rare in hyperspectral remote sensing due to acquisition constraints, making it challenging to train and evaluate these models.

A possible way to overcome the scarcity of data is to rely on synthetic data for training models. Generating such data in the field of hyperspectral imaging has been little explored and remains a challenging task. Audebert et al. [17] demonstrated that GANs can be used to generate realistic, class-conditioned hyperspectral samples, despite known issues like overfitting and training instability. Liu et al. [18] introduced a diffusion-based method to create synthetic HSIs from RGB images and the USGS Spectral Library V7 [19], with a particular focus on capturing spectral variability in the resulting synthetic images. However, their approach remains limited by the availability and completeness of spectral libraries.

In the field of computer vision, the use of synthetic data is much more common, and many works have been devoted to this topic, mostly for classification, estimation or detection tasks, relying for instance on simplified object generation [20] or more recently text-to-image models [21]. For image restoration tasks, it was recently proposed to rely on a simple occlusion-based geometric model, the dead leaves model [22], [23], to perform fully synthetic training of restoration models [24]. Dead leaves models offer a simple framework for simulating edges and homogeneous regions by overlapping opaque objects and effectively reproduce non-Gaussian statistics observed in natural images. Experiments performed in [24] show that convolutional neural networks trained exclusively on dead leaves images can achieve competitive performance for the denoising and super-resolution of natural images.

Inspired by these advances, we propose to adapt this concept to hyperspectral remote sensing images with a particular attention to urban scenes. In this work, we introduce a new framework for generating synthetic abundances images based on the dead leaves model, tailored to the characteristics of low-resolution remote sensing data. This approach enables the training of super-resolution neural networks without relying on any real high-resolution hyperspectral ground truth data, thus removing a major bottleneck in supervised learning. The contributions of this study are threefold:

- 1) We demonstrate the feasibility of training super-resolution networks for hyperspectral images entirely on synthetic data. This strategy enables unsupervised learning, as no paired real ground-truth data are required,

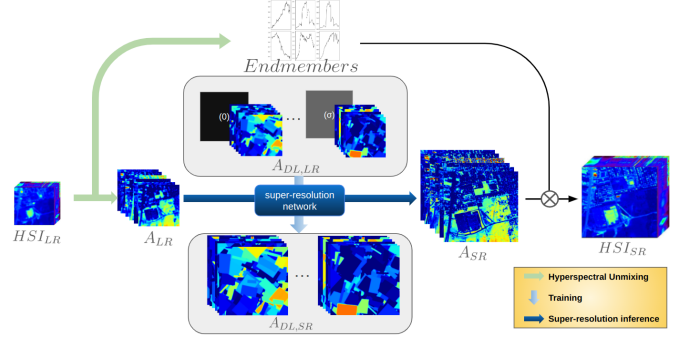


Fig. 1. Structure of the proposed method: The super-resolution network is trained with synthetic pairs ($A_{DL,SR}, A_{DL,LR}$) and then used to super-resolve A_{LR} into A_{SR} .

thereby overcoming the common limitation of scarce or unavailable references.

- 2) We introduce a synthetic HS data generation process designed specifically for remote sensing scenarios, and show that it leads to competitive super-resolution results.
- 3) We propose to generate synthetic HSI through hyperspectral unmixing, which serves as a form of spectral compression. This approach is both lightweight and computationally efficient, significantly reducing the cost and complexity of data synthesis.

This article is organized as follows: Section II describes the proposed method and Section III presents the ablation studies, the experimental results and discussion.

II. PROPOSED METHOD

A. Approach Overview

Super-resolution consists in obtaining a high spatial resolution hyperspectral image $HSI_{HR} \in \mathbb{R}^{H \times W \times L}$ from a low-resolution image $HSI_{LR} \in \mathbb{R}^{h \times w \times L}$, where h, w, H , and W (with $h < H$ and $w < W$) denote the spatial dimensions, and L is the spectral dimension. Despite its simplicity and associated limitations [25], we assume that each pixel in the HSI can be decomposed using the following linear hyperspectral unmixing model:

$$HSI_{LR}(i, j, l) = \sum_{m=1}^M A_{LR}(i, j, m) \cdot S(m, l) + N_{LR}(i, j, l) \quad (1)$$

where $A_{LR} \in \mathbb{R}^{h \times w \times M}$ and $S \in \mathbb{R}^{M \times L}$ represent the abundances and the endmembers of the low-resolution HSI, respectively, M the number of materials and $N_{LR} \in \mathbb{R}^{h \times w \times L}$ is an additive Gaussian white noise. In practice, we apply the Minimum Volume (MinVol) hyperspectral unmixing method on HSI_{LR} [26] to extract the endmembers S . Then, to limit reconstruction errors and to simplify the calculation of correlated noise described below, the abundances A_{LR} are computed using the least squares method.

Based on this decomposition, the main idea of our method is to generate a large number of synthetic abundances $A_{DL,LR} \in \mathbb{R}^{h \times w \times M}$ and $A_{DL,HR} \in \mathbb{R}^{H \times W \times M}$ from A_{LR} , using the dead leaves model (DL for short). The high-resolution

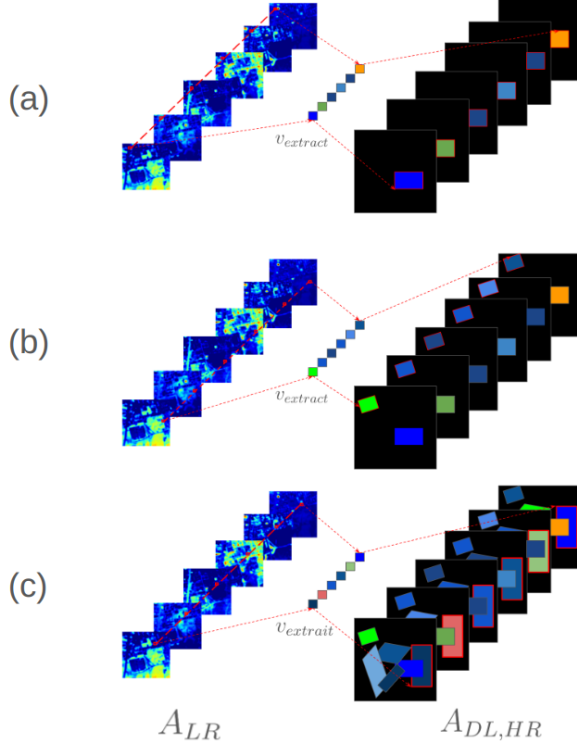


Fig. 2. Illustration of synthetic abundance generation for $A_{DL,HR}$ using the 1st, 2nd, and 3rd value columns of $v_{extract}$ in (a), (b), and (c), respectively. In (c), an example highlights the occlusion mechanism: a newly added leaf is partially covered by a previously generated one, illustrating the stacking behavior of the dead leaves model.

abundances $A_{DL,HR}$ are first generated using the DL model, while the corresponding low-resolution abundances $A_{DL,LR}$ are obtained by applying a PSF simulated through Gaussian blurring and bicubic downsampling. To improve the robustness of the network training process, a low correlated noise $N_{A,LR} \in \mathbb{R}^{h \times w \times M}$ is added to a randomly selected subset of the low-resolution abundances $A_{DL,LR}$. The synthetic pairs $(A_{DL,HR}, A_{DL,LR})$ are then used to train a super-resolution neural network. During inference, the abundances A_{LR} of the HSI to be super-resolved are fed into the network to estimate the super-resolved abundances A_{SR} . The final super-resolution hyperspectral image HSI_{SR} is reconstructed using $HSI_{SR}(i, j, l) = \sum_{m=1}^M A_{SR}(i, j, m) \cdot S(m, l)$. The structure of our method is summarized in Fig. 1.

The following sections describe in detail the process of generating synthetic abundances, adding noise and the super-resolution network.

B. Synthetic Abundance Generation by the Dead Leaves model

The main idea of the dead leaves model is to generate an image by sequentially superimposing random shapes (called leaves) at random positions, thereby mimicking the process of dead leaves falling from a tree [22], [27]. This model was in particular shown to be a powerful way to reproduce important statistics of natural images [23], [28], [29]. The shapes can be defined using random shape models, and their positions

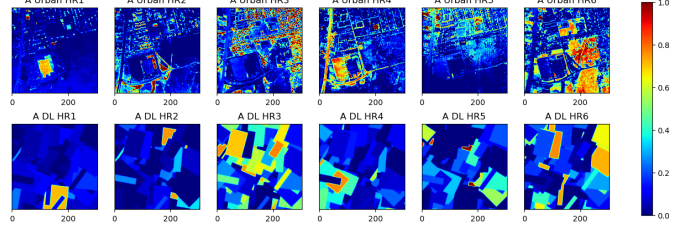


Fig. 3. Comparison between real urban abundance (Top) and synthetic dead leaves abundance (Bottom).

Algorithm 1 Synthetic Abundance Generation with the Dead Leaves Model

Require: Real abundance $A_{LR} \in \mathbb{R}^{h \times w \times M}$, target resolution (H, W)
Output: Synthetic high-resolution abundances $A_{DL,HR}$ and low-resolution abundances $A_{DL,LR}$

- 1: Initialize $A_{DL,HR} \leftarrow 0 \in \mathbb{R}^{H \times W \times M}$
- 2: Initialize $Mask \leftarrow \emptyset$
- 3: **while** $\#Mask < HW$ **do**
- 4: Sample $Leaf \leftarrow \text{Rect}(a, b, \theta) + (x, y)$
- 5: Extract a material proportion vector $\mathbf{v}_{extract} \leftarrow \text{RandomPixel}(A_{LR}) \in \mathbb{R}^M$
- 6: **for** $(x, y) \in Leaf \setminus Mask$ **do**
- 7: $A_{DL,HR}[x, y, :] \leftarrow \mathbf{v}_{extract}[:]$
- 8: **end for**
- 9: $Mask \leftarrow Mask \cup Leaf$
- 10: **end while**
- 11: Apply Gaussian blur: $A' \leftarrow \text{GaussianBlur}(A_{DL,HR})$
- 12: Downsample: $A_{DL,LR} \leftarrow \text{BicubicDownsample}(A')$

are given by a stationary Poisson point process (i.e., points uniformly distributed over the plane). The process is iterated until a stationary state is reached, which, in practice, can be achieved using perfect simulation techniques [30]: each new shape is placed beneath the previous ones, until every pixel is covered by at least one leaf.

In our approach, we generate synthetic abundances using the dead leaves model, following the principle outlined above. More precisely, an abundance map is generated by sequentially superimposing shapes bearing random abundance values (in \mathbb{R}^M). When a given pixel is covered by a random shape, it is given the abundance values of this shape, therefore prescribing its M material values in the abundance map (see Fig. 2). Given the urban context of HSIs in remote sensing, the use of rectangular leaves appears well-suited. Each leaf is characterized by a vector $(a, b, \theta, \mathbf{v}, x, y)$, where a and b define the dimensions of the rectangle, θ its orientation, $\mathbf{v} \in [0, 1]^M$ the abundance values assigned to the leaf and (x, y) the spatial coordinates of its center. The values a and b are independently drawn from a uniform distribution over $[2 \times \text{scale factor}, \min(H, W)/3]$, ensuring variability in the leaf sizes. The value θ is uniformly drawn in the interval $[0^\circ, 45^\circ]$, capturing all possible orientations due to the symmetry of the shapes.

To preserve realistic abundance statistics within the dead leaves framework, the values \mathbf{v} assigned to each synthetic

abundance are sampled by randomly selecting a pixel from A_{LR} that contains a material distribution $v_{extract}$ (see Fig. 2). This strategy ensures realistic material proportions in the generated maps, as illustrated in Fig. 3. The detailed implementation of this approach is provided in Algorithm 1.

C. Noise modeling

Adding noise to synthetic images is essential for enhancing the robustness of models trained on synthetic abundance. Assuming additive Gaussian white noise N_{LR} , and introducing the pseudo-inverse of the endmember matrix S^+ , the observation model becomes:

$$HSI_{LR}(i, j, l) = \sum_{m=1}^M \left[A_{LR}(i, j, m) + \sum_{l'=1}^L N_{LR}(i, j, l') \cdot S^+(l', m) \right] \cdot S(m, l) \quad (2)$$

This shows that the noise effect can be viewed as a direct perturbation $N_A = \sum_{l'=1}^L N_{LR}(i, j, l') \cdot S^+(l', m)$ applied to the abundance. Rather than aiming to explicitly train the network for denoising, the objective here is to increase its robustness to slight input variations. To this end, we introduce a small additive Gaussian noise N_{LR} , whose standard deviation σ follows the distribution $\sigma \sim \sigma_{\max} - \text{Exp}(\lambda)$, where σ_{\max} corresponds to the maximum noise level just above the quantization threshold of HSIs. The resulting abundance-space noise N_A is then applied to half of the synthetic abundance $A_{DL,LR}$. During training, the network learns to super-resolve both clean and slightly corrupted inputs (i.e., $A_{DL,LR}$ or $A_{DL,LR} + N_A$) into their corresponding high-resolution counterparts $A_{DL,SR}$.

D. Super-resolution Network

The super-resolution network MCNet (short for Mixed 3D/2D Convolutional Network) is a state-of-the-art supervised CNN initially developed for direct super-resolution of HSIs [16]. As the name suggests, it combines both 2D and 3D convolutional layers: the 2D layers focus on spatial feature extraction, while the 3D layers jointly capture spatial and spectral information. To adapt the network to our framework, we follow the approach of FFDNet [31] by appending a noise level map as an additional input channel, filled with the noise standard deviation. This results in an input with $M + 1$ channels, where M denotes the number of materials. This enables the network to adapt to varying noise levels and improves robustness during training.

III. EXPERIMENTS

This section presents a comprehensive evaluation of the proposed method through a series of experiments. First, in III-A, we detail the experimental setup, including the datasets, preprocessing steps, training protocols, and evaluation metrics. Then, in III-B, we provide a comparative analysis with state-of-the-art supervised super-resolution methods, highlighting the effectiveness of our unsupervised approach. The final

settings of our method are made according to the studies found in III-C, III-D and III-E. III-C explores the impact of different hyperspectral unmixing strategies through an ablation study. III-D focuses on analyzing the contributions and design choices of the dead leaves model for synthetic data generation. Finally, III-E investigates the impact of noise addition during training and its influence on network robustness.

A. Datasets & Setup

The proposed approach was evaluated on three widely used hyperspectral datasets:

- **Urban:** This dataset was captured by the Hyperspectral Digital Image Collection Experiment (HYDICE) sensor. It consists of 307×307 pixels across 210 spectral bands ranging from 400 to 2500 nm. After discarding noisy and corrupted bands, 162 bands are retained for evaluation.
- **Pavia University:** Acquired by the ROSIS-3 airborne optical sensor in 2003, this image comprises 610×340 pixels with a ground sampling distance (GSD) of 1.3 meters. It covers a spectral range of 430–840 nm distributed over 115 bands. Twelve bands affected by noise and water vapor absorption are removed. In this study, we focus on a 340×340 pixel region from the lower part of the image, using the remaining 103 bands.
- **Chikusei:** Captured by the VNIR-C sensor, the original image has a resolution of 2517×2335 pixels over 128 spectral bands. For our experiments, we randomly select a 500×500 pixel subregion.

To evaluate the performance of the proposed method, we apply down-sampling factors of $\times 2$, $\times 3$, and $\times 4$. The low-resolution hyperspectral images HSI_{LR} are generated using a Gaussian blur followed by bicubic down-sampling. The standard deviation of the Gaussian filter is set to $\sigma = 2, 3$, and 4 for each respective down-sampling factor and the filter size is truncated to 6σ to comply with the Shannon–Nyquist sampling criterion.

For each dataset and each training phase, we generate 5,000 synthetic high-resolution abundance maps $A_{DL,HR}$ of size $W \times H \times 6$, where W and H denote the spatial dimensions of the corresponding dataset. The associated low-resolution abundances $A_{DL,LR}$ are obtained by applying the appropriate PSF. Among these, 2,500 abundances are corrupted with noise following the protocol described in the previous section: for each sample synthetic image, a different noise level is randomly selected above the limit of quantification, following a decreasing exponential distribution.

The network is trained for 200 epochs on the corresponding synthetic dataset using the L1 loss function and the Adam optimizer, with a fixed learning rate of 0.0001. The other network-related parameters remain unchanged from the initial version proposed in MCNet. Performance is assessed using three metrics, where X denotes the reference high-resolution hyperspectral image and Y denotes the reconstructed image:

- Peak Signal-to-Noise Ratio (PSNR), defined as

$$\text{PSNR} = 10 \log_{10} \left(\frac{\text{MAX}^2}{\text{MSE}} \right) \quad (3)$$

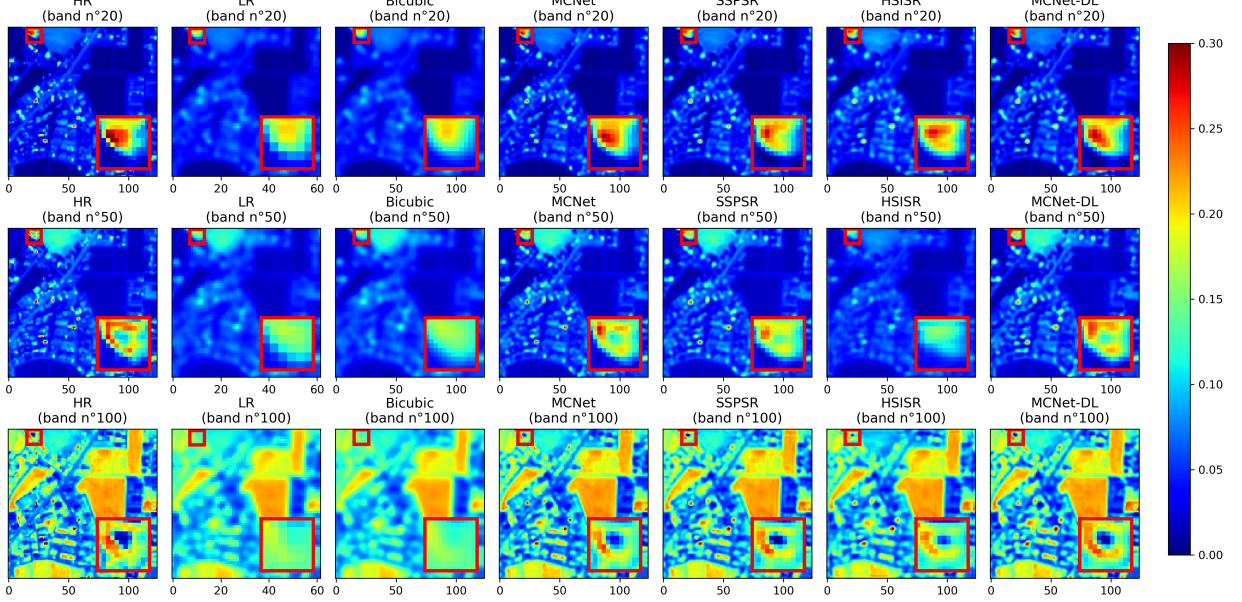


Fig. 4. Visual comparison at bands 20, 50, and 100 of a **Chikusei** patch with a $\times 2$ scaling factor: high-resolution reference (HR), low-resolution (LR), and super-resolved (SR) images generated using bicubic interpolation, MCNet, SSPSR, HSISR, and MCNet-DL.

where MAX is the maximum possible pixel value and

$$\text{MSE} = \frac{1}{HWL} \sum_{i=1}^H \sum_{j=1}^W \sum_{l=1}^L (X(i, j, l) - Y(i, j, l))^2$$

with H , W , and L denoting the height, width, and number of spectral bands, respectively.

- Spectral Angle Mapper (SAM), which computes the average spectral angle between corresponding spectral vectors in X and Y :

$$\text{SAM} = \frac{1}{HW} \sum_{i=1}^H \sum_{j=1}^W \cos^{-1} \left(\frac{\sum_{l=1}^L X(i, j, l) \cdot Y(i, j, l)}{\|X(i, j, .)\|_2 \cdot \|Y(i, j, .)\|_2} \right) \quad (4)$$

where $X(i, j, .)$ and $Y(i, j, .)$ denote the spectral vectors at pixel location (i, j) .

- Error Relative Global Adimensional Synthesis (ERGAS), given by

$$\text{ERGAS} = 100 \cdot \frac{d}{r} \cdot \sqrt{\frac{1}{l} \sum_{l=1}^L \left(\frac{\text{RMSE}_l}{\mu_l} \right)^2} \quad (5)$$

where

$$\text{RMSE}_l = \sqrt{\frac{1}{HW} \sum_{i=1}^H \sum_{j=1}^W (X(i, j, l) - Y(i, j, l))^2}$$

and μ_l is the mean value of band l in Y , while $\frac{d}{r}$ is the spatial resolution ratio between LR and HR images.

Note that the ablation studies in III-C, III-D and III-E are only carried out on the Urban dataset, focusing on the most challenging super-resolution setting, namely $\times 4$.

B. Comparison with the State-of-the-Art Methods

We compare our method, trained exclusively on a fully synthetic dataset, against state-of-the-art (SOTA) SISR methods: MCNet [16], SSPSR [14], and HSISR [15]. Bicubic interpolation is also included as a baseline. It is worth noting that all these SOTA methods are supervised, which makes the comparison more favorable to them, since they benefit from access to paired training data, unlike our approach.

To construct the training data, the dataset considered is divided into 16 non-overlapping patches. For each SOTA method, 16 independent training sessions are conducted: in each session, one patch is used exclusively for evaluation, while the remaining 15 serve as training data. This procedure, which relies on an artificial partitioning of the data, offers favorable learning conditions for supervised methods and thus favors them. However, such a setup is unrealistic in real-world applications.

In contrast, our method is trained solely on the synthetic dead leaves dataset composed of 5,000 abundances. Although our unsupervised approach allows evaluation over the entire image, we adopt the same patch-based evaluation protocol for fair comparison with SOTA methods. It is important to note that this choice modifies the quantitative results compared to those reported in the ablation studies.

Tables I summarize the average performance over the 16 evaluation patches for each method, each metric and each studied scale factors. Similarly, Figures 4, 5, and 6 provide some visual comparisons on a representative patch for each of these scale factors. Quantitatively, MCNet-DL achieves state-of-the-art results in the majority of cases across all datasets and scale factors. While MCNet-DL slightly underperforms MCNet on the $\times 2$ scale for Chikusei and Pavia University, particularly on mSAM and mERGAS, it consistently outperforms all other methods. It is important to highlight that MCNet benefits

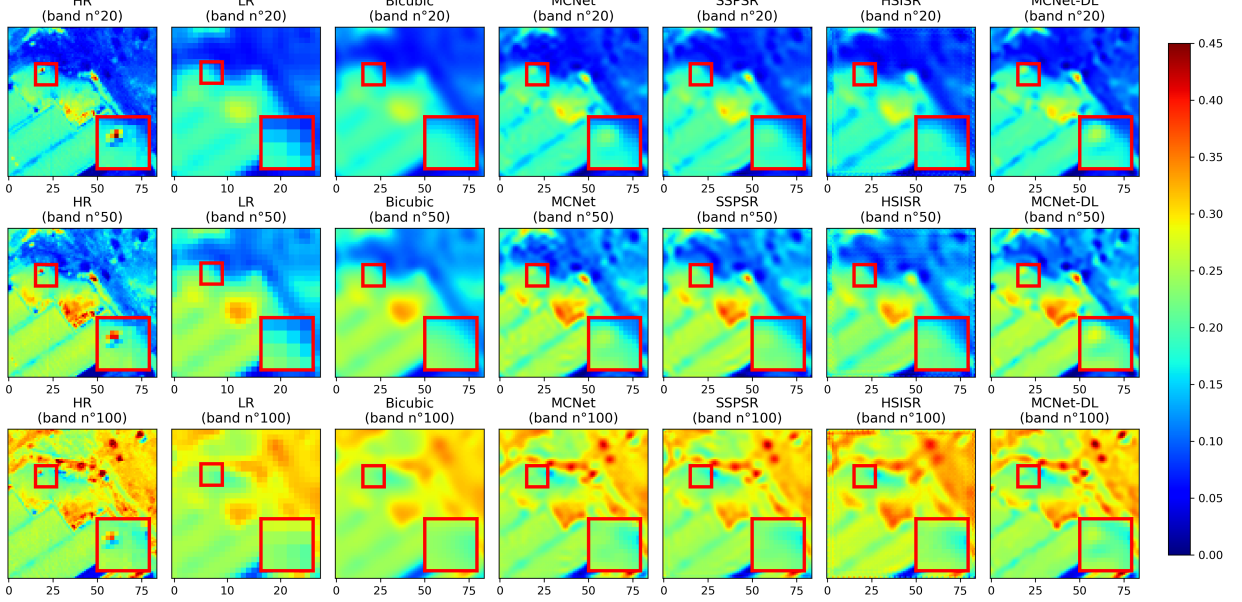


Fig. 5. Visual comparison at bands 20, 50, and 100 of a **Pavia University** patch with a $\times 3$ scaling factor: high-resolution reference (HR), low-resolution (LR), and super-resolved (SR) images generated using bicubic interpolation, MCNet, SSPSR, HSISR, and MCNet-DL.

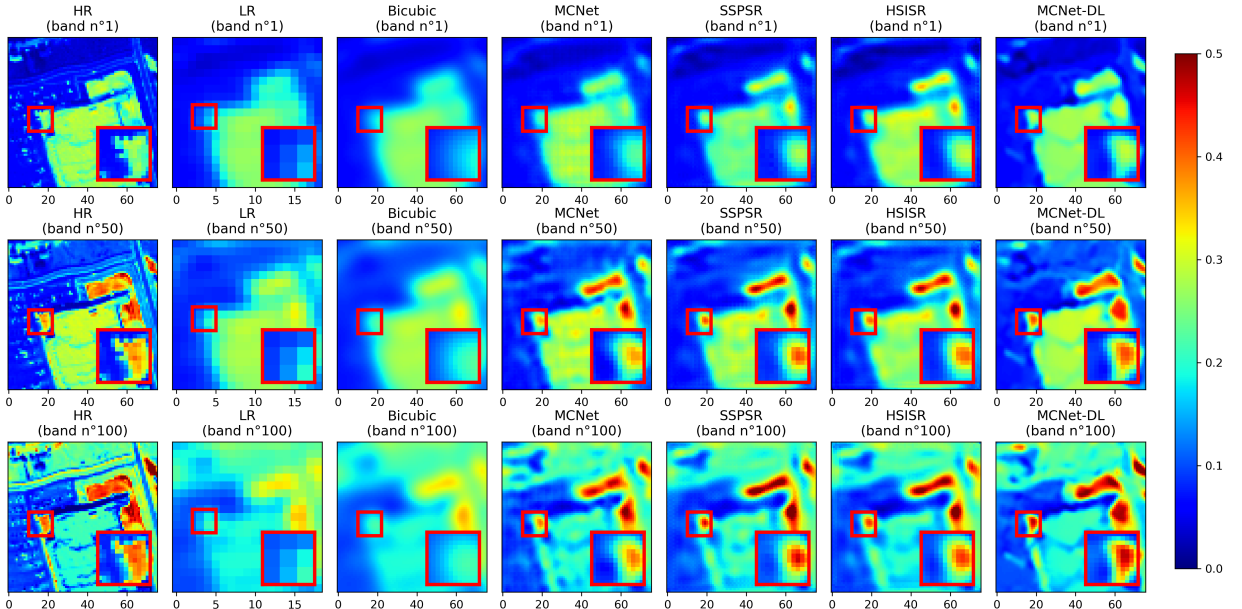


Fig. 6. Visual comparison at bands 1, 50, and 100 of a **Urban** patch with a $\times 4$ scaling factor: high-resolution reference (HR), low-resolution (LR), and super-resolved (SR) images generated using bicubic interpolation, MCNet, SSPSR, HSISR, and MCNet-DL.

from a highly favorable and supervised training setup, relying on real data from the same scene being evaluated, which constitutes an unrealistic condition in practical applications. In contrast, MCNet-DL is trained in a fully unsupervised manner. Moreover, on the more challenging $\times 3$ and $\times 4$ scales, MCNet-DL clearly surpasses MCNet across all metrics and datasets, highlighting the efficiency of our synthetic-data-based approach. Visually, MCNet-DL reconstructs more accurate spatial details and preserves spectral information better than all other methods. These improvements are especially noticeable in high-frequency regions and complex scenes, as illustrated

in the qualitative examples.

C. Hyperspectral Unmixing

This section aims to highlight the importance of hyperspectral unmixing in the proposed framework, using the Urban dataset as a benchmark. To this end, we compare several endmember extraction strategies, including a simple Principal Component Analysis (PCA) decomposition, a classical blind unmixing method known as MinVol [26], and a deep learning-based approach, CNNAEU, proposed by Pálsson et al. [32].

TABLE I
AVERAGE SUPER-RESOLUTION PERFORMANCE ACROSS SCALES ($\times 2, \times 3, \times 4$) ON THREE HYPERSPECTRAL DATASETS, COMPARING SOTA SUPERVISED METHODS WITH OUR UNSUPERVISED MCNET-DL TRAINED SOLELY ON SYNTHETIC DATA.

Scale	Method	Urban			Pavia University			Chikusei		
		mPSNR \uparrow	mSAM \downarrow	mERGAS \downarrow	mPSNR \uparrow	mSAM \downarrow	mERGAS \downarrow	mPSNR \uparrow	mSAM \downarrow	mERGAS \downarrow
$\times 2$	Bicubic	26.46	14.79	7.87	29.10	11.08	5.91	34.39	13.24	8.08
	MCNet	30.05	9.85	5.27	33.02	7.11	3.93	39.63	7.36	4.60
	SSPSR	29.43	10.55	5.62	31.59	8.34	4.61	38.79	8.22	5.21
	HSISR	29.27	10.29	5.50	27.98	11.66	7.10	32.78	13.99	10.66
$\times 3$	MCNet-DL	30.47	9.33	4.93	33.09	7.30	4.02	39.29	7.86	4.78
	Bicubic	24.99	17.54	9.30	27.24	13.60	7.15	32.51	16.41	9.93
	MCNet	27.12	13.67	7.28	29.76	10.23	5.49	35.25	12.14	7.41
	SSPSR	26.51	14.70	7.52	29.37	10.78	5.88	35.36	11.78	7.31
$\times 4$	HSISR	26.79	14.41	7.75	28.14	12.15	6.76	32.29	16.09	10.71
	MCNet-DL	28.05	12.19	6.41	30.75	9.42	5.03	36.53	10.67	6.52
	Bicubic	24.31	19.09	10.14	26.33	15.21	7.93	31.52	18.36	11.02
	MCNet	25.76	16.26	8.61	28.19	12.17	6.46	33.28	15.16	9.16
	SSPSR	25.13	17.08	8.84	27.64	12.53	6.79	33.40	15.01	8.95
	HSISR	25.41	17.01	8.84	25.74	15.12	9.05	29.42	21.01	14.86
	MCNet-DL	26.54	14.71	7.67	29.34	11.06	5.84	34.99	12.92	7.85

TABLE II

SUPER-RESOLUTION PERFORMANCE ($\times 4$) USING DIFFERENT METHODS OF UNMIXING/DECOMPOSITION ON THE URBAN DATASET WITH $M = 6$.

Decomposition method	PSNR \uparrow	SAM \downarrow	ERGAS \downarrow
endmembers GT	26.19	14.89	7.44
MinVol	25.75	15.73	7.85
CNNAEU	24.83	18.23	9.19
PCA	14.55	67.33	25.70

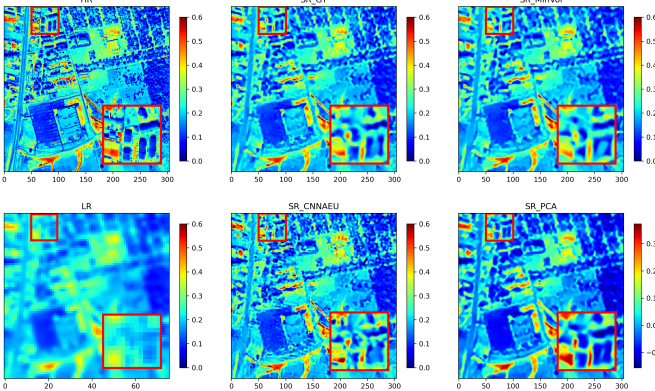


Fig. 7. Visual comparison at band 100: high-resolution reference (HR), Low-resolution (LR), and super-resolved (SR) images obtained using endmembers from ground truth (GT), MinVol, CNNAEU, and PCA-based decomposition.

We also include the commonly used ground-truth endmembers, annotated by Zhu [33], as a reference.

The Urban dataset is particularly suited for this analysis, as it includes ground-truth versions with different numbers of endmembers: $M = 4$, $M = 5$, and $M = 6$. In this study, we focus on the case with $M = 6$ endmembers, as it better preserves spectral diversity and reduces compression artifacts typically associated with lower-dimensional representations.

As outlined above, regardless of the unmixing method employed, we retain only the extracted spectral signatures and apply a least-squares procedure to estimate the corresponding abundance. This approach limits reconstruction error and facilitates the analysis of spatially correlated noise in the

TABLE III
SUPER-RESOLUTION PERFORMANCE ($\times 4$) USING DIFFERENT SYNTHETIC ABUNDANCE GENERATION STRATEGIES OR SUPER-RESOLUTION NETWORKS ON THE URBAN DATASET WITH $M = 6$.

SR strategy	PSNR \uparrow	SAM \downarrow	ERGAS \downarrow
MCnet-DL	25.75	15.73	7.85
MCnet-Nat	20.91	26.76	13.54
MCnet-DirichletDL	24.47	18.51	9.26
RDN-DL	23.83	19.91	9.85

abundance domain, enabling a fair and consistent evaluation of super-resolution performance across methods.

Table II summarizes the quantitative super-resolution performance achieved with different endmember extraction strategies, while Figure 7 provides a visual illustration of the corresponding reconstruction results. As expected, using ground-truth endmembers gives the best results for all measurements. Among blind unmixing methods, the MinVol approach achieves performance close to the ground truth, demonstrating its relevance. Although CNNAEU still outperforms PCA, its accuracy remains slightly lower than that of GT and MinVol, and the reconstruction exhibits more noticeable artefacts. In contrast, the PCA-based decomposition yields significantly poorer results, with dynamics that are markedly shifted and tend to produce negative values. Moreover, its components often lack clear physical or visual relevance, making them less informative for interpretation. These results underscore the value of dedicated unmixing techniques in extracting meaningful spectral signatures. Since ground-truth endmembers are not always accessible, we rely on the MinVol method for spectral extraction.

D. Ablation studies on dead leaves

In this section, we present ablation studies for the dead leaves model, focusing on three key aspects: (1) the relevance of using dead leaves, (2) the importance of preserving the material distribution from real low-resolution abundance A_{LR} , and (3) the model's adaptability across different super-

resolution network architectures. Table III summarizes all the tests performed for the section ablation studies.

1) *The relevance of using dead leaves:* The idea is to demonstrate the relevance of the dead leaves model for generating synthetic abundance. To assess this, by using MCnet, we compare DL abundances (denoted as MCnet-DL) to an alternative approach that uses natural image statistics. Specifically, we leverage the DIV2K dataset [34], which contains a wide range of high-resolution natural images. By extracting random patches from these images and interpreting them as proxy abundance distributions (denoted as MCnet-Nat).

Quantitative results from Table III clearly show that MCnet-DL significantly outperforms MCnet-Nat across all evaluation metrics. The dead leaves model not only provides higher spatial fidelity (as reflected by the PSNR) but also better preserves spectral characteristics, as indicated by the lower SAM and ERGAS values. These results support the relevance of the DL model, whose structured and layered composition produces training data that more faithfully captures the physical and spatial constraints inherent in real hyperspectral mixtures. This leads to more accurate and robust super-resolution performance. In comparison, although natural image statistics offer high variability, they do not reflect the underlying semantics of abundance mixing, ultimately resulting in less effective learning.

2) *The material distribution:* We now assess the importance of preserving the material distribution observed in real data. To this end, we compare MCnet-DL, which samples each leaf's value V from real low-resolution abundance A_{LR} , to MCnet-DirichletDL, a variant where V is instead drawn from a uniform Dirichlet distribution $\text{Dir}(1, \dots, 1)$. In this setting, for each new leaf, an N -dimensional abundance vector $\mathbf{v} \sim \text{Dir}(1, \dots, 1)$ is sampled, and its m^{th} component is assigned to the leaf at layer m . All geometric parameters (a, b, θ, x, y) remain identical between the two methods.

Results in Table III show that MCnet-DL consistently outperforms MCnet-DirichletDL across all metrics. These results clearly demonstrate that leveraging the true material distribution from A_{LR} leads to more realistic and effective training data, whereas sampling from a uniform Dirichlet prior introduces unlikely combinations of materials that hinder super-resolution performance.

3) *Adaptability to various super-resolution networks:* One significant advantage of the dead leaves dataset is its versatility across various super-resolution architectures. To evaluate this property, we replace MCnet, a network specifically designed for hyperspectral image processing, with RDN [35], a general-purpose super-resolution model originally developed for natural images. RDN employs a residual architecture and is capable of super-resolving single-channel grayscale images, making it naturally adaptable to inputs with $M + 1$ channels as required by our method. The resulting configuration is denoted as RDN-DL.

According to the results in Table III, RDN-DL achieves competitive performance across all metrics, albeit slightly lower than that of MCnet-DL. This difference in performance is anticipated, given that RDN does not inherently exploit the spectral correlations specific to hyperspectral data. Nev-

TABLE IV
SUPER-RESOLUTION PERFORMANCE ($\times 4$) UNDER DIFFERENT TRAINING CONFIGURATIONS ON CLEAN AND NOISY TEST DATA (URBAN DATASET, $M = 6$)

Test Dataset	DL Configuration	PSNR \uparrow	SAM \downarrow	ERGAS \downarrow
Urban	Clean	26.10	15.13	7.58
	Noisy	25.45	16.44	8.19
	HalfMix	25.85	15.62	7.84
	StdAware	25.75	15.73	7.85
Noisy Urban	Clean	16.94	39.42	22.45
	Noisy	25.43	16.49	8.22
	HalfMix	23.86	20.02	9.82
	StdAware	25.57	16.12	8.04

ertheless, the strong performance of RDN-DL highlights the benefits conferred by the DL training data. Overall, these results demonstrate that the dead leaves model offers a flexible and reliable basis for hyperspectral super-resolution tasks, regardless of the particular architecture used.

In summary: The dead leaves model proves to be a powerful and versatile tool for synthetic data generation in hyperspectral image super-resolution. It not only generates physically realistic spatial structures that better match real abundance but also preserves meaningful material statistics and supports diverse network architectures. These advantages collectively enable improved model performance, robustness, and generalization.

E. Discussion on Noise and network training robustness

We address the question of noise by showing that adding a small amount of noise during training is essential for network stability. Without it, models trained exclusively on clean synthetic data become overly sensitive to minor fluctuations at test time, especially when applied to slightly noisy real-world abundance. This leads to the appearance of ringing artifacts, as the network mistakenly treats these small variations as meaningful details to super-resolve. By introducing noises during training, we regularize the network's behavior and effectively eliminate such artifacts, resulting in more robust and reliable reconstructions.

To investigate this effect, 2 test datasets were prepared. The first is the Urban dataset, which has been used throughout the ablation studies, with a scale factor of $\times 4$ and $M = 6$ endmembers. The second is a noisy version of the Urban dataset, where additive Gaussian noise corresponding to a PSNR of 60dB was applied to the low-resolution HSI. This noise level is extremely low, close to the quantization limit, and remains imperceptible to the human eye. Regarding the training dataset configuration, 4 networks were trained independently and under identical conditions on different datasets. The first dataset consists exclusively of noiseless DL abundances (Clean). The second dataset contains the same DL abundances, but all corrupted with random Gaussian noise at a PSNR level above the quantization threshold (Noisy). The third dataset is a balanced mixture composed of 50% Clean and 50% Noisy samples (HalfMix). Finally, the fourth dataset includes the same abundances as HalfMix, with an additional

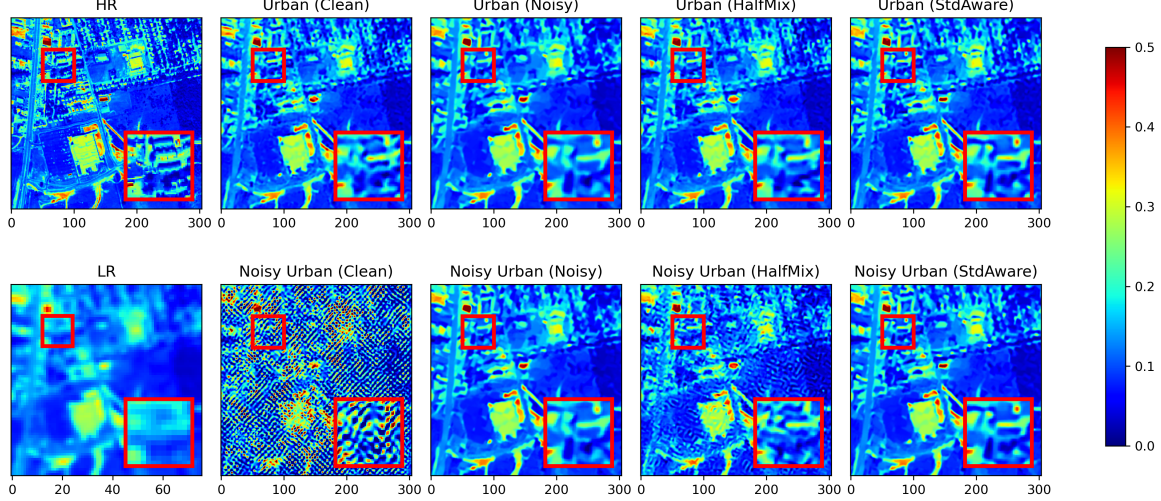


Fig. 8. Visual Comparison at band 50 of Super-Resolved Abundance under Different Training Configurations (Urban dataset, $M = 6$, $\times 4$)

noise level map concatenated to the abundance, increasing the number of channels to $M+1$, as described in previous sections (StdAware).

An analysis of both the visual results (Fig.8) and the quantitative metrics (Tab.IV) reveals that, for the Urban dataset, super-resolution performance remains highly satisfactory. Training exclusively on Clean data yields the best results, while the Noisy training exhibits a slight performance decline, consistent with the nature of the respective datasets. However, when evaluated on the Noisy Urban test set, the detrimental effects of noise become evident: networks trained on Clean data display pronounced artifacts, and the HalfMix configuration only partially mitigates these effects, leading to a noticeable degradation in performance. These observations underscore the importance of introducing noise during training to enhance robustness. Nonetheless, training exclusively on noisy data leads to a significant loss of performance when applied to clean images. Consequently, the StdAware configuration emerges as the most effective compromise, offering improved resilience to noise while preserving high reconstruction quality on noiseless data. When the noise level is unavailable, an acceptable alternative is to train the neural network with the HalfMix strategy.

IV. CONCLUSION

In this work, we introduced a novel approach for the super-resolution of hyperspectral remote sensing images. By designing a framework based entirely on synthetic data, our method operates in an unsupervised manner, thus addressing the challenges related to limited datasets and the absence of ground truth. Significant efforts were dedicated to enhancing the realism of synthetic data, thereby improving both the performance and robustness of network training. Experimental results on three widely used hyperspectral datasets validated the effectiveness of our approach across various down-sampling scales, with performance metrics confirming the model ability to preserve both spatial structures and spectral fidelity.

Moreover, the proposed framework offers considerable flexibility, both in the generation of synthetic data and in the choice of super-resolution networks, allowing for a wide range of adaptations in network design, dataset creation, and their combinations. Nevertheless, the method relies on prior knowledge of the sensor's PSF to remain effective. One perspective could involve integrating PSF estimation within the framework. Another promising perspective would be to design synthetic abundance datasets with sufficient generality to enable super-resolution of remote sensing abundance independently of sensor-specific characteristics.

ACKNOWLEDGMENTS

The work was partially supported by Agence de l'Innovation de Défense – AID - via Centre Interdisciplinaire d'Etudes pour la Défense et la Sécurité – CIEDS - (project 2023 - ALIA).

REFERENCES

- [1] M. Fahes, C. Kervazo, J. Bobin, and F. Tupin, "Unrolling palm for sparse semi-blind source separation," *arXiv preprint arXiv:2112.05694*, 2021.
- [2] X. Wu, D. Hong, and J. Chanussot, "Uiu-net: U-net in u-net for infrared small object detection," *IEEE Transactions on Image Processing*, vol. 32, pp. 364–376, 2022.
- [3] S. J. Mills, M. P. G. Castro, Z. Li, J. Cai, R. Hayward, L. Mejias, and R. A. Walker, "Evaluation of aerial remote sensing techniques for vegetation management in power-line corridors," *IEEE Transactions on Geoscience and Remote Sensing*, vol. 48, no. 9, pp. 3379–3390, 2010.
- [4] J. Yao, B. Zhang, C. Li, D. Hong, and J. Chanussot, "Extended vision transformer (exvit) for land use and land cover classification: A multimodal deep learning framework," *IEEE Transactions on Geoscience and Remote Sensing*, vol. 61, pp. 1–15, 2023.
- [5] N. Yokoya, C. Grohfeldt, and J. Chanussot, "Hyperspectral and multispectral data fusion: A comparative review of the recent literature," *IEEE Geoscience and Remote Sensing Magazine*, vol. 5, no. 2, pp. 29–56, 2017.
- [6] J. M. Bioucas-Dias, A. Plaza, N. Dobigeon, M. Parente, Q. Du, P. Gader, and J. Chanussot, "Hyperspectral unmixing overview: Geometrical, statistical, and sparse regression-based approaches," *IEEE journal of selected topics in applied earth observations and remote sensing*, vol. 5, no. 2, pp. 354–379, 2012.
- [7] K. Zheng, L. Gao, W. Liao, D. Hong, B. Zhang, X. Cui, and J. Chanussot, "Coupled convolutional neural network with adaptive response function learning for unsupervised hyperspectral super resolution," *IEEE Transactions on Geoscience and Remote Sensing*, vol. 59, no. 3, pp. 2487–2502, 2020.

[8] D. Hong, J. Yao, C. Li, D. Meng, N. Yokoya, and J. Chanussot, “Decoupled-and-coupled networks: Self-supervised hyperspectral image super-resolution with subpixel fusion,” *IEEE Transactions on Geoscience and Remote Sensing*, vol. 61, pp. 1–12, 2023.

[9] T. Akgun, Y. Altunbasak, and R. M. Mersereau, “Super-resolution reconstruction of hyperspectral images,” *IEEE Transactions on Image processing*, vol. 14, no. 11, pp. 1860–1875, 2005.

[10] H. H. Bauschke and J. M. Borwein, “On projection algorithms for solving convex feasibility problems,” *SIAM review*, vol. 38, no. 3, pp. 367–426, 1996.

[11] Y. Yuan, X. Zheng, and X. Lu, “Hyperspectral image superresolution by transfer learning,” *IEEE Journal of Selected Topics in Applied Earth Observations and Remote Sensing*, vol. 10, no. 5, pp. 1963–1974, 2017.

[12] S. Mei, X. Yuan, J. Ji, Y. Zhang, S. Wan, and Q. Du, “Hyperspectral image spatial super-resolution via 3d full convolutional neural network,” *Remote Sensing*, vol. 9, no. 11, p. 1139, 2017.

[13] J. Li, R. Cui, B. Li, Y. Li, S. Mei, and Q. Du, “Dual 1d-2d spatial-spectral cnn for hyperspectral image super-resolution,” in *IGARSS 2019–2019 IEEE International Geoscience and Remote Sensing Symposium*. IEEE, 2019, pp. 3113–3116.

[14] J. Jiang, H. Sun, X. Liu, and J. Ma, “Learning spatial-spectral prior for super-resolution of hyperspectral imagery,” *IEEE Transactions on Computational Imaging*, vol. 6, pp. 1082–1096, 2020.

[15] K. Li, D. Dai, and L. Van Gool, “Hyperspectral image super-resolution with rgb image super-resolution as an auxiliary task,” in *Proceedings of the IEEE/CVF Winter Conference on Applications of Computer Vision*, 2022, pp. 3193–3202.

[16] Q. Li, Q. Wang, and X. Li, “Mixed 2d/3d convolutional network for hyperspectral image super-resolution,” *Remote sensing*, vol. 12, no. 10, p. 1660, 2020.

[17] N. Audebert, B. Le Saux, and S. Lefèvre, “Generative adversarial networks for realistic synthesis of hyperspectral samples,” in *IGARSS 2018–2018 IEEE International Geoscience and Remote Sensing Symposium*. IEEE, 2018, pp. 4359–4362.

[18] L. Liu, B. Chen, H. Chen, Z. Zou, and Z. Shi, “Diverse hyperspectral remote sensing image synthesis with diffusion models,” *IEEE Transactions on Geoscience and Remote Sensing*, vol. 61, pp. 1–16, 2023.

[19] R. F. Kokaly, R. N. Clark, G. A. Swayze, K. E. Livo, T. M. Hoefen, N. C. Pearson, R. A. Wise, W. Benzel, H. A. Lowers, R. L. Driscoll *et al.*, “Usgs spectral library version 7,” US Geological Survey, Tech. Rep., 2017.

[20] A. Dosovitskiy, P. Fischer, E. Ilg, P. Hausser, C. Hazirbas, V. Golkov, P. Van Der Smagt, D. Cremers, and T. Brox, “Flownet: Learning optical flow with convolutional networks,” in *Proceedings of the IEEE international conference on computer vision*, 2015, pp. 2758–2766.

[21] Y. Tian, L. Fan, P. Isola, H. Chang, and D. Krishnan, “Stablerep: Synthetic images from text-to-image models make strong visual representations learners,” *Advances in Neural Information Processing Systems*, vol. 36, pp. 48 382–48 402, 2023.

[22] G. Matheron, “Modele séquentiel de partition aléatoire,” Technical report, CMM, Tech. Rep., 1968.

[23] L. Alvarez, Y. Gousseau, and J.-M. Morel, “The size of objects in natural and artificial images,” in *Advances in Imaging and Electron Physics*. Elsevier, 1999, vol. 111, pp. 167–242.

[24] R. Achddou, Y. Gousseau, and S. Ladjal, “Fully synthetic training for image restoration tasks,” *Computer Vision and Image Understanding*, vol. 233, p. 103723, 2023.

[25] C. Kervazo, N. Gillis, and N. Dobigeon, “Provably robust blind source separation of linear-quadratic near-separable mixtures,” *SIAM Journal on Imaging Sciences*, vol. 14, no. 4, pp. 1848–1889, 2021.

[26] N. Gillis, “Successive nonnegative projection algorithm for robust non-negative blind source separation,” *SIAM Journal on Imaging Sciences*, vol. 7, no. 2, pp. 1420–1450, 2014.

[27] C. Bordenave, Y. Gousseau, and F. Roueff, “The dead leaves model: a general tessellation modeling occlusion,” *Advances in applied probability*, vol. 38, no. 1, pp. 31–46, 2006.

[28] A. B. Lee, D. Mumford, and J. Huang, “Occlusion models for natural images: A statistical study of a scale-invariant dead leaves model,” *International Journal of Computer Vision*, vol. 41, pp. 35–59, 2001.

[29] Y. Gousseau and F. Roueff, “Modeling occlusion and scaling in natural images,” *Multiscale Modeling & Simulation*, vol. 6, no. 1, pp. 105–134, 2007.

[30] W. S. Kendall and E. Thöennes, “Perfect simulation in stochastic geometry,” *Pattern recognition*, vol. 32, no. 9, pp. 1569–1586, 1999.

[31] K. Zhang, W. Zuo, and L. Zhang, “Ffdnet: Toward a fast and flexible solution for cnn-based image denoising,” *IEEE Transactions on Image Processing*, vol. 27, no. 9, pp. 4608–4622, 2018.

[32] B. Palsson, M. O. Ulfarsson, and J. R. Sveinsson, “Convolutional autoencoder for spectral-spatial hyperspectral unmixing,” *IEEE Transactions on Geoscience and Remote Sensing*, vol. 59, no. 1, pp. 535–549, 2020.

[33] F. Zhu, “Hyperspectral unmixing: ground truth labeling, datasets, benchmark performances and survey,” *arXiv preprint arXiv:1708.05125*, 2017.

[34] E. Agustsson and R. Timofte, “Ntire 2017 challenge on single image super-resolution: Dataset and study,” in *Proceedings of the IEEE conference on computer vision and pattern recognition workshops*, 2017, pp. 126–135.

[35] Y. Zhang, Y. Tian, Y. Kong, B. Zhong, and Y. Fu, “Residual dense network for image super-resolution,” in *Proceedings of the IEEE conference on computer vision and pattern recognition*, 2018, pp. 2472–2481.



Xinxin Xu received the engineering degree from Institut d’Optique Graduate School, France, in 2023. He is currently pursuing the Ph.D. degree with LTCI, Télécom Paris, Institut Polytechnique de Paris, Palaiseau, France, under the supervision of Yann Gousseau, Christophe Kervazo and Saïd Ladjal.

His research focuses on hyperspectral image super-resolution, with applications in remote sensing.



and video processing.



medical imaging.



Saïd Ladjal received a diplôme de magister from École normale supérieure in 2000 including a Masters degree in computer science, engineering degree from Télécom Paris in 2002 and Ph.D degree in applied mathematics from École normale supérieure de Cachan in 2005.

He is currently a Professor with Télécom Paris. His research interests are on mathematical modeling for images and computational photography with applications to remote sensing, general image restoration and medical imaging.